(I) *Dynamic adaptation.* Because of motion complexity, tumours can have amplitude changes, baseline shifting and period changes. The thresholds Θ_c and Λ_c for testing velocity change and amplitude will change dynamically during on-line data processing. At the beginning, these thresholds are initialized to default values. As more and more data arrive, the thresholds change to adapt to the most recent breathing patterns. In our one-dimensional implementation, the threshold on amplitude, Λ_c, is initialized to 4 mm for superior–inferior motion more than 7 mm. As data are processed, Λ_c tracks one-third of the magnitude of the EX or IN states, averaged over the last four breathing periods. Similarly, Θ_c is initialized to 4.5 mm s^{-1}, and dynamically changes to match one quarter of the average velocity of the EX state.

3. Materials

We performed this study retrospectively using lung tumour movement data of patients treated using the real-time tumour-tracking radiation therapy (RTRT) system at Hokkaido University (Seppenwoolde *et al* 2002, Shirato *et al* 2000a, 2000b). In this system, a 2 mm or 1.5 mm diameter gold marker is inserted into or near the lung tumour using image guided implantation. The system can detect the actual marker position at a rate of 30 Hz using two x-ray imaging systems. It uses fluoroscopy image processor units to determine the 3D position of the implanted marker and employs automatic pattern recognition of the markers in real time. The geometric accuracy of the tumour-tracking system is better than 1.5 mm. Lung tumour motion data of 42 patients treated between 2001 and 2002 were analysed. From these, 23 patients with breathing amplitude greater than 7 mm were identified and used to evaluate fitting quality and to analyse motion patterns.

A qualitative examination of the tumour motion patterns and signal quality of 23 patients shows that there are significant differences between patients. An example of the breathing signals from six different patients is shown in figure 9. Figure 9(a) shows a breathing pattern that is regular in both period and amplitude. Figure 9(b) shows the motion of a tumour where the breathing frequency changes over time. Figure 9(c) illustrates a breathing pattern with base line shifts. Figure 9(d) displays a tumour motion with amplitude changes. Figure 9(e) highlights the fact that the raw tracking signal is often noisy due to cardiac motion. Figure 9(f) demonstrates a breathing pattern where both the exhale home position and the amplitude drift over time. These motion patterns are well characterized by our finite state model.

A more detailed observation shows that there are other breathing cycle patterns, as illustrated in figure 10. A breathing cycle with three breathing states, as shown in figure 10(a), is the most general case, comprising approximate 85% of our breathing data. About 10% of the patients only have exhale and inhale states, or with a very short end-of-exhale state, which is illustrated in figure 10(b). About 5% patients breathe with an additional relaxation state after inhale as shown in figure 10(c). Figure 10(d) displays a special breathing pattern, where there are two end-of-exhale states, separated by a short inhale-like state. Some patients have more complicated breathing signals which incorporate several breathing state patterns. As illustrated in figure 10(e), a patient can alternate between 2-state, 3-state and 4-state motions.

4. Results and discussion

In this section, we will discuss the advantages of this finite state model, the quality of our on-line implementation, an application of the analysis results and some drawbacks of our model.

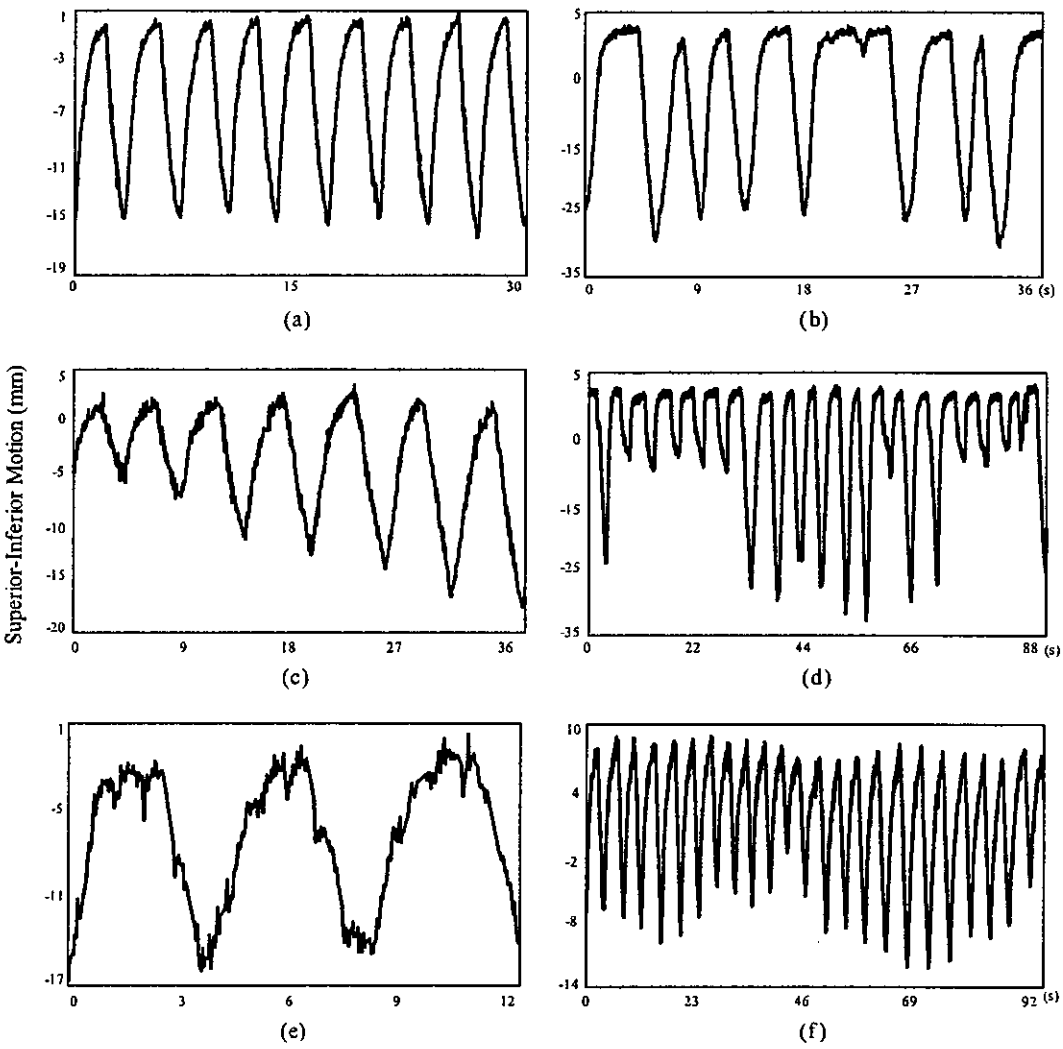

Figure 9. Tumour motion and data quality: (a) regular breathing, (b) frequency changes, (c) baseline shifts, (d) amplitude changes, (e) cardiac motion and (f) combinations.

The idea of using three states to model a regular breathing cycle has several advantages. First, it fits well with our natural understanding of tumour respiratory motion. Second, it provides a convenient way to characterize the motion of the EOE state, usually used as gating window in gated treatment. The model also provides a convenient way to summarize and compare statistical information for different states, which can be used in dynamic treatment planning during real-time radiotherapy or radiosurgery. Third, the piecewise linear representation of raw streams saves storage and will produce fast retrieval of historical medical information. Fourth, our implementation algorithm of the finite state model works in an on-line fashion. The algorithm only requires constant space and runs in linear time. The line segment of current respiration can be determined in real time. The average processing time for each new measurement is less than 1 ms. The quick response time is a big advantage for its application in real-time radiotherapy. Finally, this model is suitable for both on-line subsequence similarity matching and offline patient similarity analysis.

The root mean square (RMS) errors of the on-line fitting for 23 different patients and their average RMS errors are shown in figure 11. The average RMS error is less than 1 mm

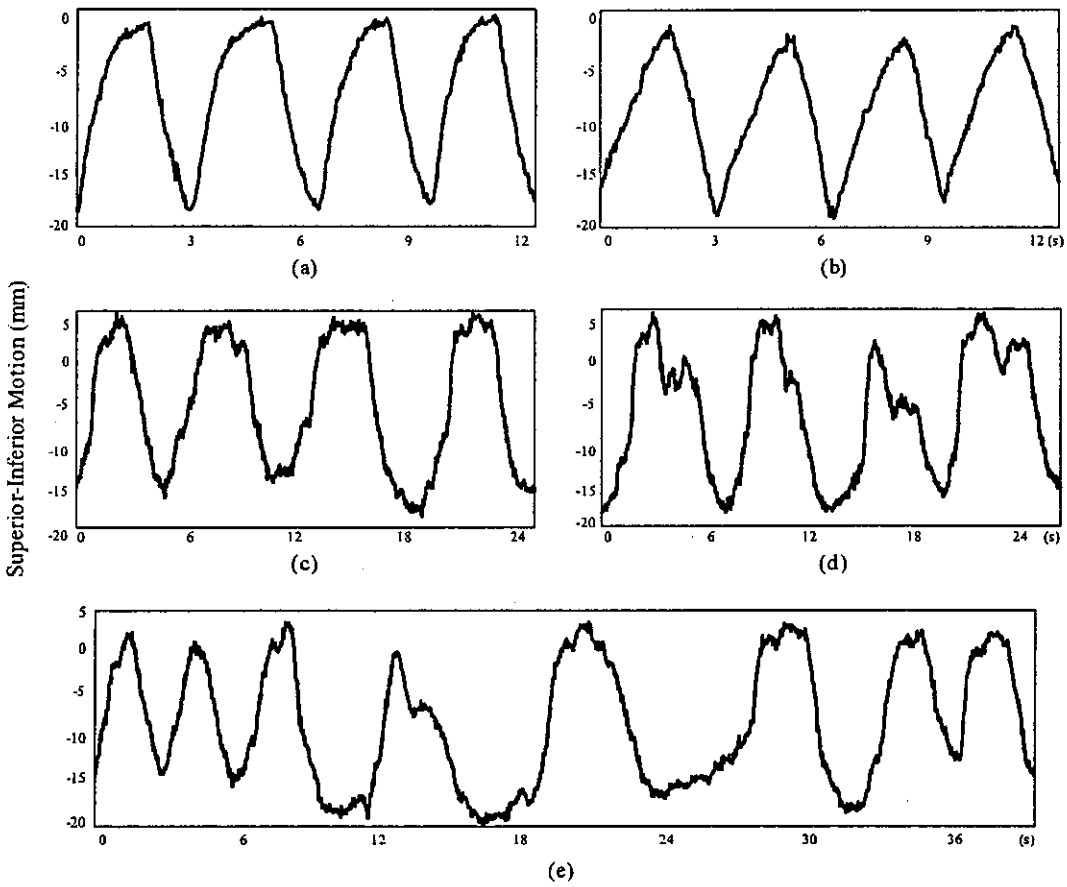

Figure 10. Common and unusual breathing patterns: (a) three breathing states, (b) two breathing states, (c) four breathing states, (d) special breathing states and (e) combinations of all breathing states.

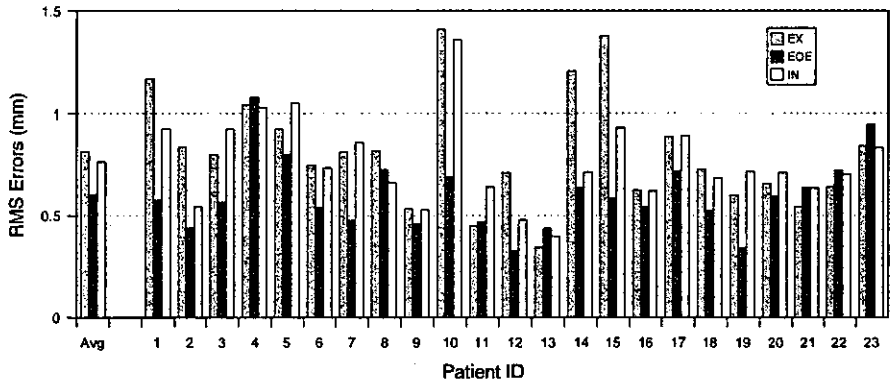

Figure 11. Fidelity of our model to raw data.

on average and less than 1.5 mm for all patients. As demonstrated in figure 11, most patients have the smallest RMS error in the EOE state. The RMS errors for exhale and inhale states are quite similar, with a little variation for different patients. This pattern of the RMS errors can be explained by the motion pattern of tumours. Tumours have less movement in the EOE state, while larger movements in exhale and inhale states.

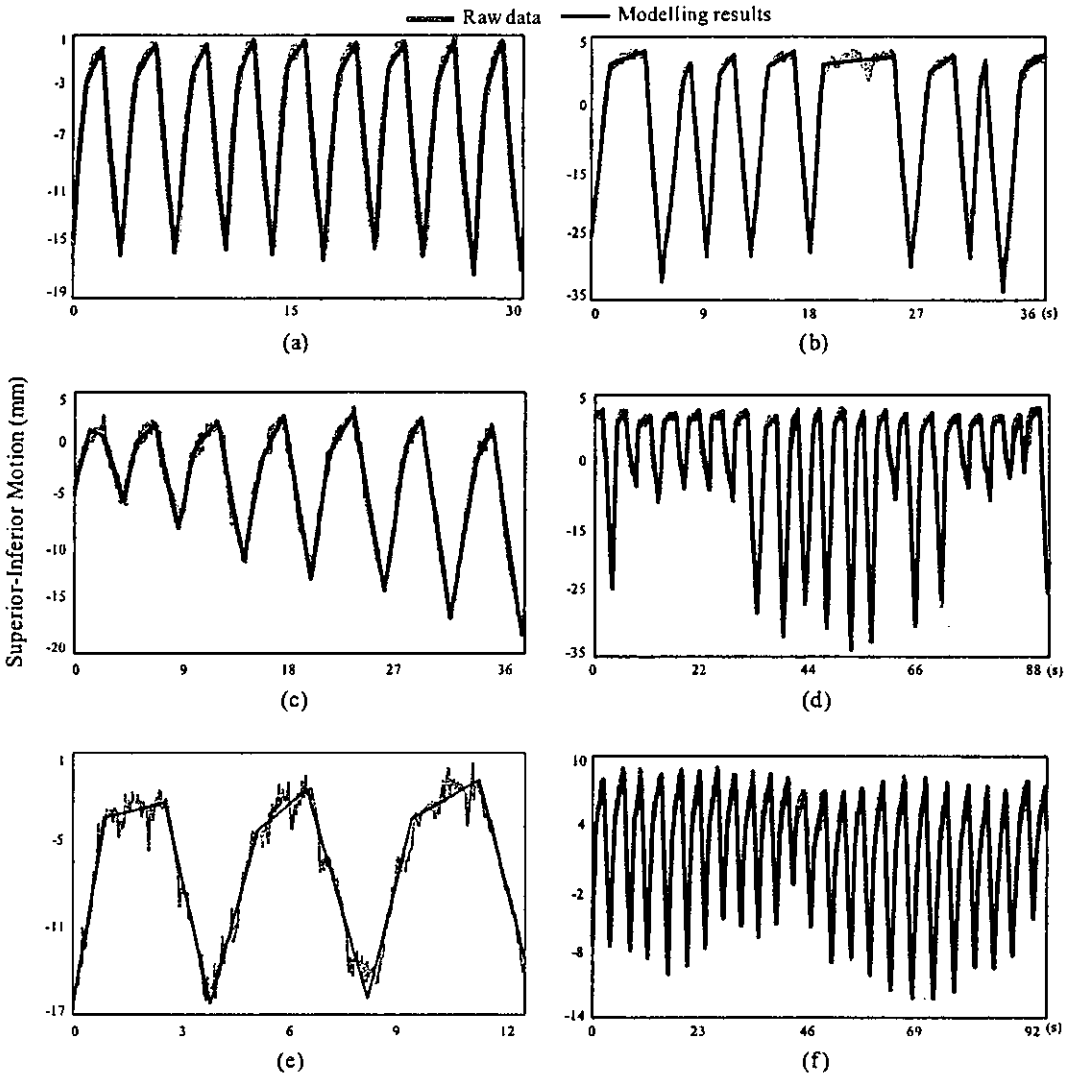

Figure 12. Modelling results of different breathing patterns and data qualities: (a) regular breathing, (b) frequency changes, (c) baseline shifts, (d) amplitude changes, (e) cardiac motion and (f) combinations.

The finite state model works not only for tumour motion with regular breathing patterns, it produces good fitting results even for patients who have very complex breathing patterns, such as breathing with frequency changes, amplitude changes, base line shifting, or the combination of all the variations. It also works well for patients with different breathing cycle patterns, such as two-state, three-state, four-state, or the combinations of all the different patterns. Figures 12 and 13 display the modelling results of the respiratory motion in figures 9 and 10. The final line segments seem to be a qualitatively good representation of the raw data.

The three-state motion model gives convenient ways to summarize and analyse motion characteristics. Figure 14 presents the different breathing lengths for each state. The average time across patients shows that the EOE state is the longest breathing phase, and exhale and inhale states have shorter length. For some patients, such as patients 11 and 13, EOE is the shortest phase of breathing. Other patients have equal breathing time for each of the three states, such as patients 4 and 19. Yet other patients have the breathing time in the order of

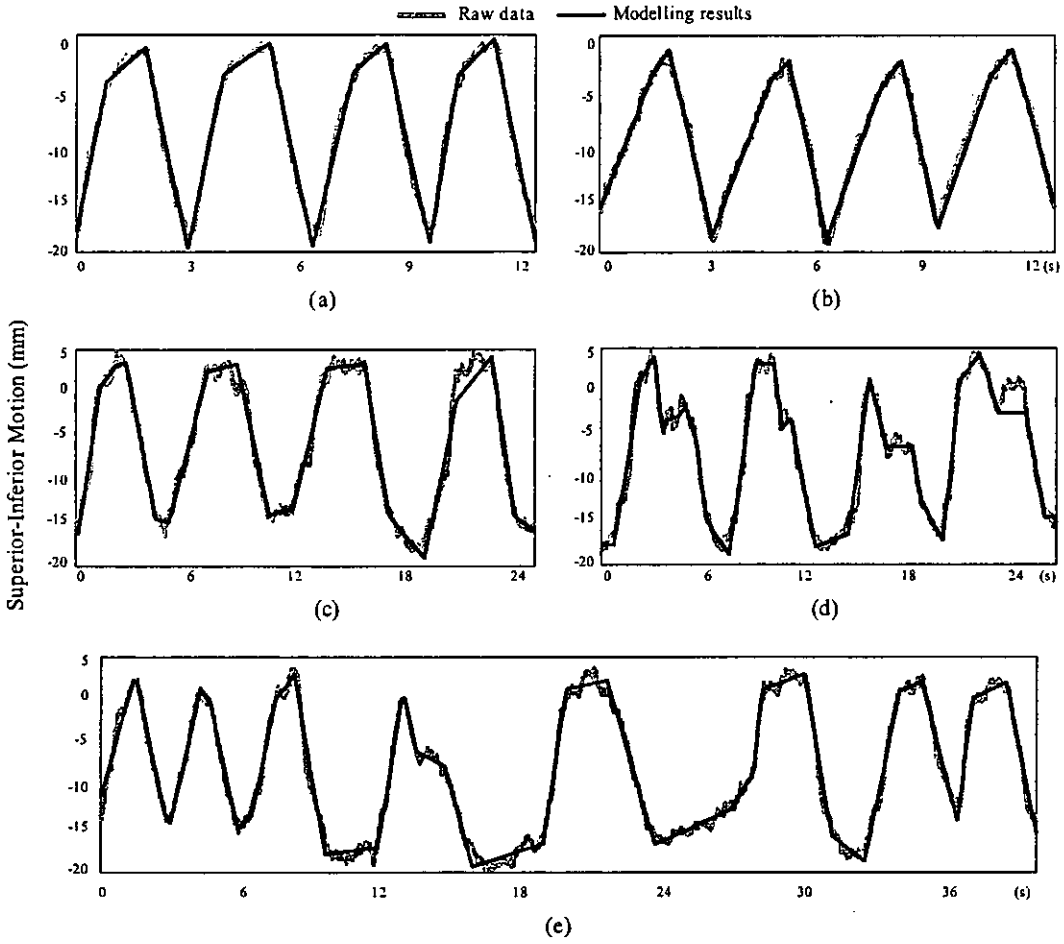

Figure 13. Modelling results for common and unusual breathing patterns: (a) three breathing states, (b) two breathing states, (c) four breathing states, (d) special breathing states and (e) combinations of all breathing states.

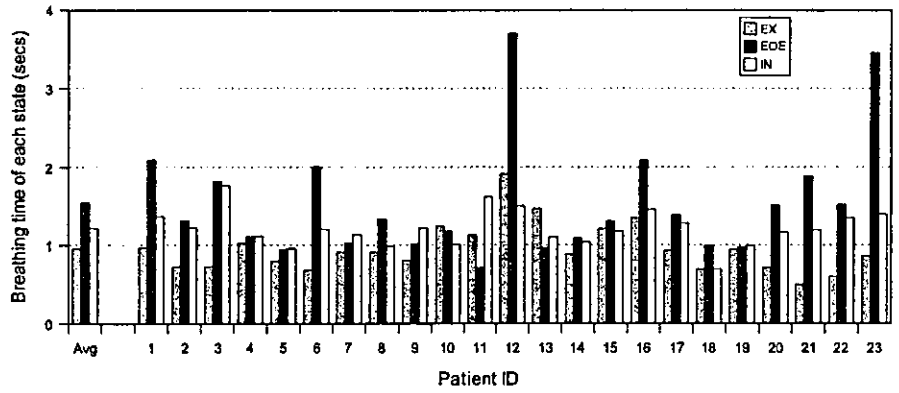

Figure 14. Average time spent in regular breathing phases.

EX < EOE < IN, such as patients 7 and 9. Examples of these differences are shown in figure 15.

There are a few patients with RMS errors more than 1 mm among the 23 patients shown in figure 11. One source of this error is patients whose exhale and inhale states are not quite

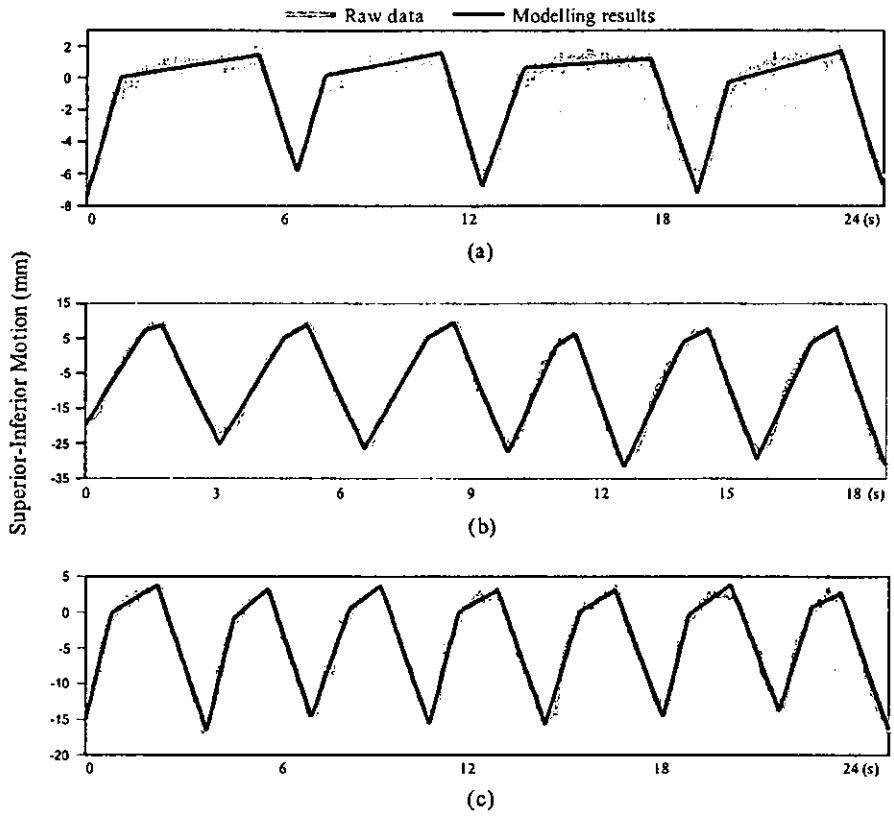

Figure 15. Different patterns of a breathing cycle: (a) longer EOE state, shorter EX and IN states, (b) shorter EOE state, longer EX and IN states and (c) lengths in the increasing order of EX, EOE and IN states.

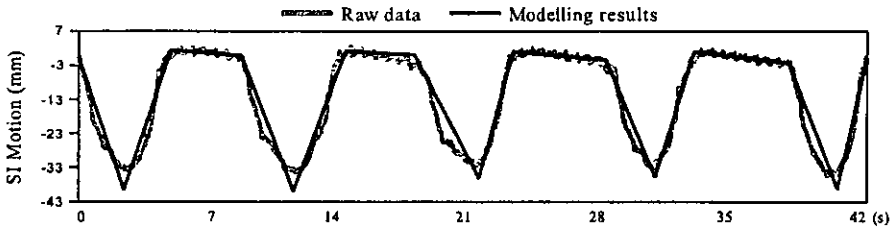

Figure 16. Nonlinear states are preferred for some breathing patterns.

linear. For example, consider the motion of patient 10, as illustrated in figure 16. Nonlinear exhale and inhale states would give a better result for this patient. Another shortcoming of our model is that it only can handle tumours with small cardiac motion. For tumours with cardiac motion more than half of the motion amplitude, our model cannot distinguish the respiratory motion from the cardiac motion. Finally, the rigid assumption of three states for one breathing period also puts limitations on the expressiveness of this model. For example, if a tumour only moves with exhale and inhale states, our method enforces the tumour to have an EOE state. It would be preferred to switch from a three-state model to a two-state model. Another example is that if a breathing period may have an additional state between the end of inhale and the beginning of exhale. Our model generates an irregular state (IRR) for the prolonged inhale state, where a four-state model will give a better understanding.

5. Conclusion

We have proposed a three-state model for respiratory tumour motion that fits the natural understanding of breathing phases, and conforms well to real patient data. We have implemented a one-dimensional version of this model in an on-line algorithm that segments the breathing signal into line segments for each state. The average root mean square error of our model is less than 1.5 mm for the patients, which demonstrates the fidelity of our model to raw data. This model and its implementation can be used for both on-line and offline data analyses. The patterns of different breathing states give useful information about patient-specific breathing. This model can be applied to internal and external motions, including tumour position, abdominal surface, diaphragm, spirometry and other surrogates.

Our future research includes several areas. One area modifies the current model to include nonlinear states, and more or less states per breathing period. We would like to address cardiac motion in the context of tumour respiratory motion. Another ongoing project is motion prediction based on the finite state model for real-time radiation therapy. A salient feature of the model is that it provides a handy base for statistics, probability analysis and database similarity matching. We are combining all these technologies in the prediction method to improve the prediction results.

Acknowledgments

This work was supported in part by NSF grant IIS-0073063, the Whitaker Foundation Grant RG-01-0175, and CenSSIS, the Center of Subsurface Sensing and Imaging Systems, under the Engineering Research Centers Program of the NSF (award number EEC-9986821).

References

Bortfeld T and Jiang S B 2004 Effects of motion on the total dose distribution *Semin. Radiat. Oncol.* **14** 41–51

Bortfeld T, Jokivarsi K, Goitein M, Kung J and Jiang S B 2002 Effects of intra-fraction motion on IMRT dose delivery: statistical analysis and simulation *Phys. Med. Biol.* **47** 2203–20

Goitein M 2004 Organ and tumour motion: an overview *Semin. Radiat. Oncol.* **14** 2–9

Jiang S B, Pope C, Aljarrah K M, Kung J, Bortfeld T and Chen G T Y 2003 An experimental investigation on intra-fractional organ motion effects in lung IMRT treatments *Phys. Med. Biol.* **48** 1773–84

Keall P J, Kini V R, Vedam S S and Mohan R 2001 Motion adaptive x-ray therapy: a feasibility study *Phys. Med. Biol.* **46** 1–10

Lujan A E, Larsen E W, Balter J M and Ten Haken R K 1999 A method for incorporating organ motion due to breathing into 3D dose calculations *Med. Phys.* **26** 715–20

Mageras G S and Yorke E 2004 Deep inspiration breath hold and respiratory gating strategies for reducing organ motion in Radiation treatment *Semin. Radiat. Oncol.* **14** 65–75

Murphy M J 2004 Tracking moving organs in real time *Semin. Radiat. Oncol.* **14** 91–100

Neicu T, Shirato H, Seppenwoolde Y and Jiang S B 2003 Synchronized moving aperture radiation therapy (SMART): average tumour trajectory for lung patients *Phys. Med. Biol.* **48** 587–98

Seppenwoolde Y, Shirato H, Kitamura K, Shimizu S and Adler J R 2002 Precise and real-time measurement of 3D tumour motion in lung due to breathing and heartbeat, measured during radiotherapy *Int. J. Radiat. Oncol. Biol. Phys.* **53** 822–34

Shirato H *et al* 2000a Four-dimensional treatment planning and fluoroscopic real-time tumour tracking radiotherapy *Int. J. Radiat. Oncol. Biol. Phys.* **48** 1187–95

Shirato H *et al* 2000b Physical aspects of a real-time tumour-tracking system for gated radiotherapy *Int. J. Radiat. Oncol. Biol. Phys.* **48** 435–42

Suh Y, Yi B, Ahn S, Kim J, Lee S, Shin S and Choi E 2004 Aperture maneuver with compelled breath (AMC) for moving tumours: A feasibility study with a moving phantom *Med. Phys.* **31** 760–6

van Herk M 2004 Errors and margins in radiotherapy *Semin. Radiat. Oncol.* **14** 52–64

Int. J. Radiation Oncology Biol. Phys., Vol. 60, No. 2, pp. 607–612, 2004

0360-3016/04/$–see front matter

doi:10.1016/j.ijrobp.2004.05.042

PHYSICS CONTRIBUTION

THREE-DIMENSIONAL CONFORMAL SETUP (3D-CSU) OF PATIENTS USING THE COORDINATE SYSTEM PROVIDED BY THREE INTERNAL FIDUCIAL MARKERS AND TWO ORTHOGONAL DIAGNOSTIC X-RAY SYSTEMS IN THE TREATMENT ROOM

HIROKI SHIRATO, M.D., MASATAKA OITA, M.S., KATSUHISA FUJITA, R.T., SHINICHI SHIMIZU, M.D., RIKIYA ONIMARU, M.D., SHINJI UEGAKI, M.D., YOSHIHARU WATANABE, R.T., NORIO KATO, M.D., AND KAZUO MIYASAKA, M.D.

Department of Radiology, Hokkaido University School of Medicine, Sapporo, Japan

Purpose: To test the accuracy of a system for correcting for the rotational error of the clinical target volume (CTV) without having to reposition the patient using three fiducial markers and two orthogonal fluoroscopic images. We call this system "three-dimensional conformal setup" (3D-CSU).

Methods and Materials: Three 2.0-mm gold markers are inserted into or adjacent to the CTV. On the treatment couch, the actual positions of the three markers are calculated based on two orthogonal fluoroscopies crossing at the isocenter of the linear accelerator. Discrepancy of the actual coordinates of gravity center of three markers from its planned coordinates is calculated. Translational setup error is corrected by adjustment of the treatment couch. The rotation angles (α, β, γ) of the coordinates of the actual CTV relative to the planned CTV are calculated around the lateral (x), craniocaudal (y), and anteroposterior (z) axes of the planned CTV. The angles of the gantry head, collimator, and treatment couch of the linear accelerator are adjusted according to the rotation of the actual coordinates of the tumor in relation to the planned coordinates. We have measured the accuracy of 3D-CSU using a static cubic phantom.

Results: The gravity center of the phantom was corrected within 0.9 ± 0.3 mm (mean ± SD), 0.4 ± 0.2 mm, and 0.6 ± 0.2 mm for the rotation of the phantom from 0–30 degrees around the x, y, and z axes, respectively, every 5 degrees. Dose distribution was shown to be consistent with the planned dose distribution every 10 degrees of the rotation from 0–30 degrees. The mean rotational error after 3D-CSU was −0.4 ± 0.4 (mean ± SD), −0.2 ± 0.4, and 0.0 ± 0.5 degrees around the x, y, and z axis, respectively, for the rotation from 0–90 degrees.

Conclusions: Phantom studies showed that 3D-CSU is useful for performing rotational correction of the target volume without correcting the position of the patient on the treatment couch. The 3D-CSU will be clinically useful for tumors in structures such as paraspinal diseases and prostate cancers not subject to large internal organ motion.

Three-dimensional conformal setup, Real-time tumor-tracking radiation therapy, Fiducial marker, Setup error, Rotation correction, Rotational setup error, Real-time tumor-tracking system, Linear accelerator.

INTRODUCTION

Rotational error due to internal organ motion and setup is an important issue that has not been well understood. Van Herk *et al.* have shown that internal rotation of prostate gland was observed and that the rotation was largest around the left-right axis with the standard deviation of 4.0 degrees in the sequential measurement using computed tomography (CT) (1). Rotational setup error has been detected in the treatment of spinal schwannoma with the systematic/random error of rotation at 7.1/5.9, 6.6/4.6, and 3.0/3.1 degrees around left-right, craniocaudal, and anteroposterior, respectively (2).

A radiopaque internal fiducial marker implanted into or near the tumor has been shown to be useful for correcting translational setup error using two sets of orthogonal fluoroscopy in the treatment room (3–7). However, translational setup using only that marker would be misleading if there were rotational setup errors of the clinical target volume (CTV). When there is a large rotational error of CTV, one cannot notice it when using only one implanted marker.

Reprint requests to: Hiroki Shirato, M.D., Department of Radiology, Hokkaido University School of Medicine, North 15 West 7, Kita-ku, Sapporo 060-8638, Japan. Tel: (+81) 11-706-5975; Fax: (+81) 11-706-7876; E-mail: hshirato@radi.med.hokudai.ac.jp

This work was supported in part by a Grant-in-Aid from the Japanese Ministry of Education, Culture, Sports, Science and Technology.

Received Feb 6, 2004, and in revised form May 12, 2004. Accepted for publication May 17, 2004.

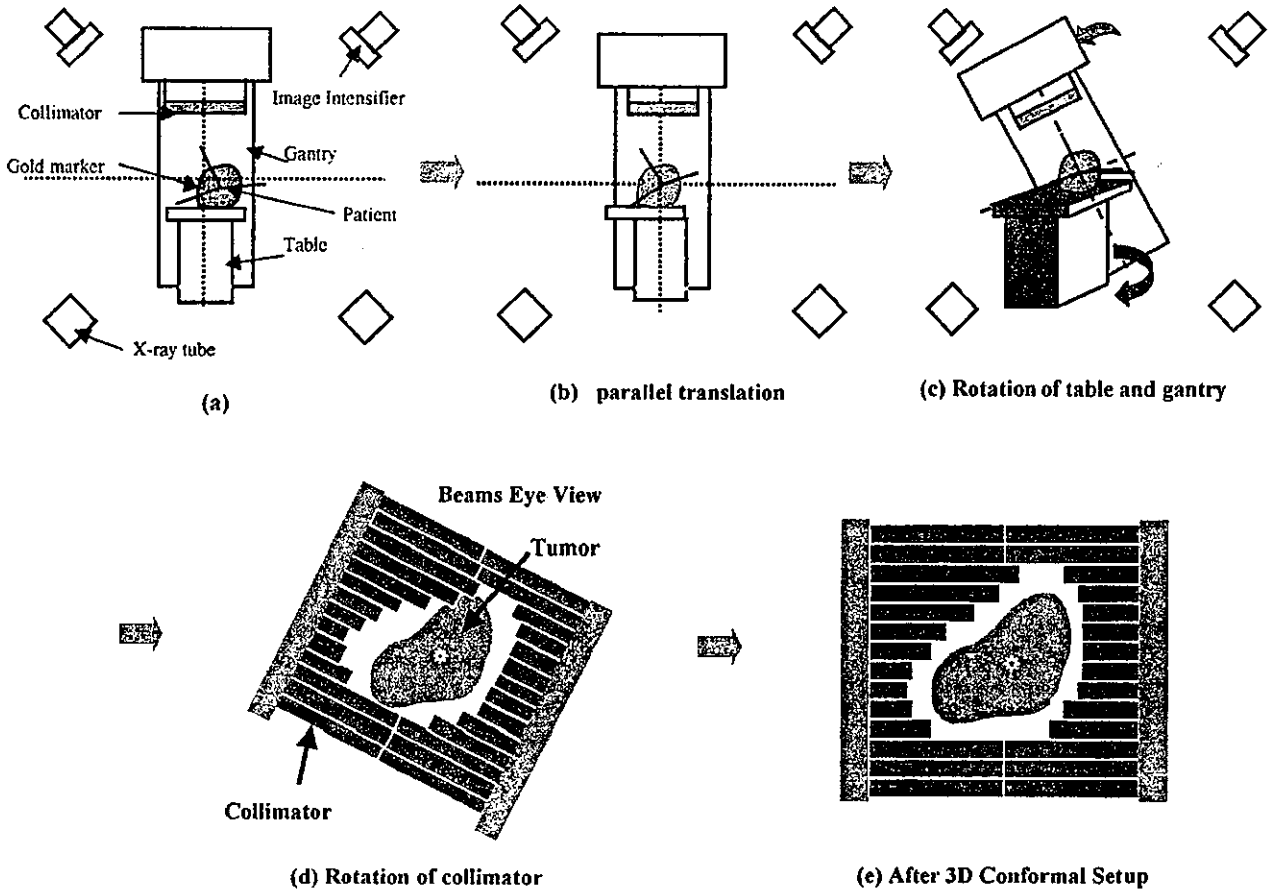

Fig. 1. Illustration of three-dimensional (3D) conformal setup. (a) The patient is manually positioned on the couch. (b) The center of gravity of three markers is translated to the planned position (three-markers translational setup). (c) Correction for the rotational error by rotating the gantry and couch around the isocenter. (d) Correction for the rotational error by rotating the collimator. (e) After performing steps (a) to (d), the relationship between the clinical target volume and beam is three-dimensionally consistent with the planned relationship.

The implantation of three markers around the CTV may be useful for the calculation and reduction of the rotational setup error. We have developed a system for reducing the rotational setup error by using three implanted markers and two sets of orthogonal fluoroscopy in the treatment room. As this procedure makes it possible to correct the three-dimensional conformality of the actual treatment, we call it "three-dimensional conformal setup" (3D-CSU) in this article.

In the present study, we tested the accuracy of 3D-CSU using a phantom and film measurement.

MATERIALS AND METHODS

The concept of the 3D-CSU is as follows (Fig. 1).

1. Three 2.0-mm gold markers are inserted into or adjacent to the CTV. The technique and its feasibility have already been published (6). Three markers should be placed in the tissue surrounding the CTV.

2. The CTV is then determined using CT images with 1–3 mm slice thickness. The planning target volume (PTV) is determined by adding a setup margin. The coordinates of the three markers relative to the target center are transferred to the setup system. The setup system calculates the coordinates of the gravity center of the triangle made by the three markers as well as the coordinates of the CTV relative to the isocenter.

3. On the treatment couch, the actual positions of the three markers are calculated based on two orthogonal fluoroscopies crossing at the isocenter of the linear accelerator. The actual position of the gravity center of the triangle made by the three markers is corrected by parallel translation of the treatment couch to be consistent with its planned position (Fig. 1). As a result, the gravity center of the CTV should be consistent with its planned position as long as migration of the marker and deformation of the CTV are negligible. The three-marker translational setup is to be more accurate than one-marker translational setup as it minimizes the adverse effect of the rotation of the CTV relative to the isocenter. Because the gravity center of the CTV matches its planned position in the three-marker translational setup, large setup error, which can occur with one-marker setup, can be avoided.

4. Rotational setup error is calculated assuming a coordinate system specific for each CTV. The actual CTV co-

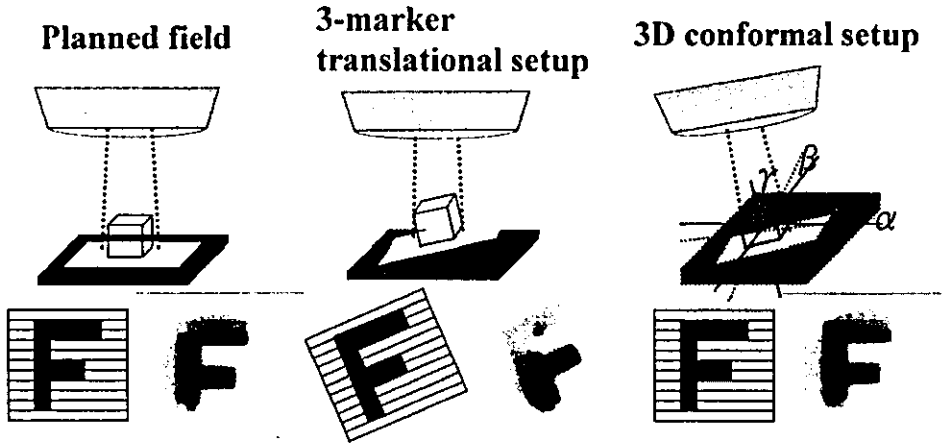

Fig. 2. Illustration of the dose distribution in the arbitrarily rotated cubic phantom with or without correction for rotation. Dose distribution measured by film on the cubic phantom with (left) no rotation, (middle) arbitrary rotation and correction by the three-marker translational setup, and (right) arbitrary rotation, calculation of the rotational angle (α, β, γ), and correction by three-dimensional (3D) conformal setup.

ordinate system is determined by the three markers in the fluoroscopic images, and the planned CTV coordinate system is determined by those in the CT images. Details of the calculation method of the rotational setup error have already been published (2). In brief, the actual CTV coordinates Σ' are expressed as $\Sigma' = M\Sigma$ where M is the direction cosine matrix and Σ represents the planned CTV coordinates. The matrix M is calculated using the inverse of matrix Σ as follows: $M = \Sigma' \Sigma^{-1}$. The rotation angles (α, β, γ) of the coordinates of the actual CTV relative to the planned CTV are calculated around the lateral (x), craniocaudal (y), and anteroposterior (z) axes of the planned CTV. The coordinate system of the linac is calibrated to the tumor's coordinates derived from the position of the three markers.

5. The angles of the gantry head, collimator, and treatment couch of the linear accelerator are adjusted according to the rotation of the actual coordinates of the tumor in relation to the planned coordinates. We call this procedure the 3D-CSU in this article. These procedures should match the actual beam's-eye view consistent with the projection of the actual CTV to the beam's direction. The 3D-CSU procedure can improve three-dimensional conformality in comparison with three-marker translational setup.

In this study, the accuracy of the three-marker translational setup and 3D-CSU were measured using the cubic phantom and film measurement. The phantom was fixed to a rotating device with a protractor, which could be intentionally rotated and stopped at a certain angle with an accuracy of 0.5 degrees. The phantom was rotated every 5 degrees around the x, y, and z axes in the experiment. The difference between the actual coordinates of the phantom's center of gravity and its calculated coordinates was measured by using three-marker translational setup from 0–30 degrees. The difference in the treatment field between the setup methods was measured by putting the film at the bottom of the phantom. The results were compared among no correction, three-marker translational setup, and 3D-CSU for the phantom rotated every 10 degrees from 0–30 degrees around the x, y, and z axes.

The actual angle of the phantom's rotation and that calculated using 3D-CSU was compared from 0–90 degrees. The values are based on three measurements for each angle from 0–90 degrees around the x, y, and z axes every 5 degrees.

RESULTS

Figure 2 illustrates the effect of 3D-CSU using an arbitrary irradiation field, "F", made by multileaf collimators. A $6.0 \times 6.0 \times 6.0$ cm^3 cubic phantom with a 2-mm fiducial marker on each corner was scanned with CT using a 1-mm slice thickness. Treatment planning was performed using a beam perpendicular to one of the phantom's surfaces. An X-ray film (XVII, Kodak, Rochester, NY) was attached to the phantom's bottom surface. First, the phantom was irradiated with a 4-MV X-ray at the position consistent with the planned position (Fig. 2, left). Second, the phantom was rotated in three dimensions to unplanned angles. After three-marker translational setup, the phantom was irradiated without correction for the rotation (Fig. 2, middle). Dose distribution to which the phantom was exposed was apparently rotated away from the planned dose distribution. Third, 3D-CSU was used, and the gantry, collimator, and couch were rotated according to the calculation. After 3D-CSU, the dose distribution was shown to be consistent with the planned dose distribution for the nonrotated phantom (Fig. 2, right).

The relationship between the phantom's rotation angle and the discrepancy of the coordinates of the gravity center of the phantom from the planned position was improved by using three-marker translational setup in comparison with the one-marker translational setup (Fig. 3). The coordinates were different from the planned coordinates considerably when only one marker was used for setup. The discrepancy

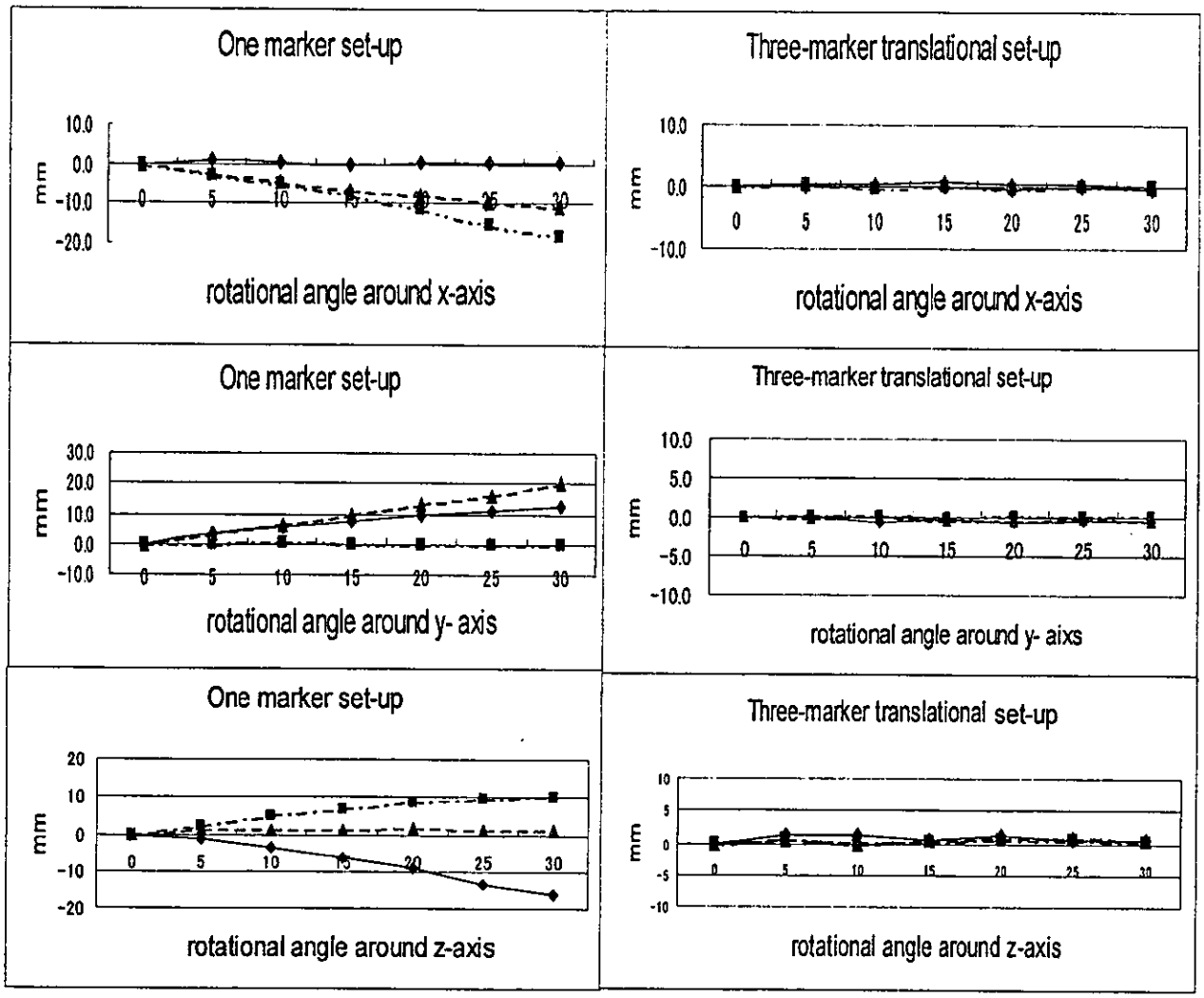

Fig. 3. Discrepancy between the planned position and the actual position of the gravity center of the phantom in (left) one-marker translational setup and (right) three-marker translational setup in the x (upper row), y (middle row), and z (lower row) directions. The discrepancy of coordinates in x-direction (squares), y-direction (triangles), and z-direction (diamonds) is shown in mm.

of the gravity center of the phantom was as large as 20 mm when the rotation angle was 30 degrees in one-marker translational setup for the 6.0 × 6.0 × 6.0 cm^3 cubic phantom. Using three-marker translational setup, the discrepancy was 0.9 ± 0.3 mm (mean ± standard deviation [SD]), 0.4 ± 0.2 mm, and 0.6 ± 0.2 mm throughout the rotation angle in the range from 0–30 degrees for the x, y, and z axes, respectively, in the gravity center of the phantom.

The differences in the treatment fields between no correction, one-marker translational setup and 3D-CSU were shown from 10–30 degrees around the x, y, and z axes (Fig. 4). The experiment showed us that a one-marker setup may reduce the rotational setup error around the y (β) and z (γ) axes in Fig. 4. However, one-marker setup may result in an alignment worse than the alignment without any correction that is seen with the rotational setup error around x axis (α) in Fig. 4. This is because the displacement of one marker can be larger than the displacement of the gravity center of the target volume in the rotational setup error. If we use the marker that moved more than the gravity center of the target volume in translational "correction," the gravity center of the target volume may be "overcorrected." Three-dimensional conformal setup was able to reduce the error due to rotation without any deterioration in translational alignment (α, β, γ; Fig. 4).

Table 1 shows the mean and SD of the angles measured with the 3D-CSU system. The mean ± SD was −0.4 ± 0.4, −0.2 ± 0.4, and 0.0 ± 0.5 degrees for α, β, and γ, respectively, from 0–90 degrees.

DISCUSSION

The setup system using two orthogonal diagnostic fluoroscopies and one internal fiducial marker has been shown to be useful for reducing translational setup error (4). However, this system was vulnerable to misalignment due to

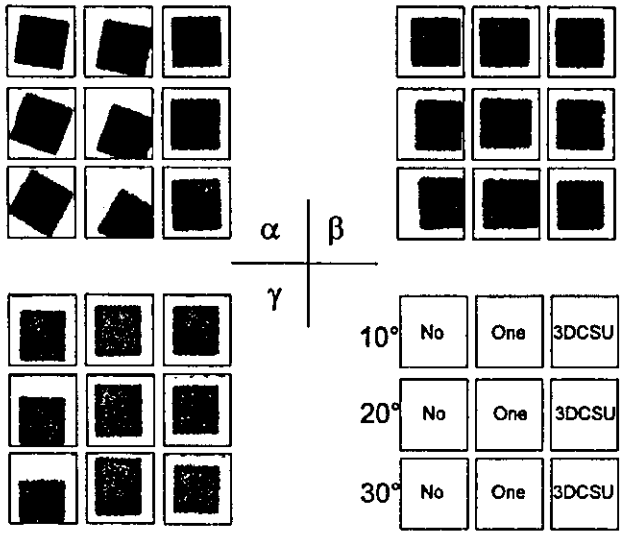

Fig. 4. The differences in dose distribution at the surface of the phantom, which was rotated from 10–30 degrees around the x (α), y (β), and z axes (γ). The dose distribution was measured without correction, with one-marker translational setup of the phantom, and with three-dimensional conformal setup (3DCSU) of the phantom.

rotation of the CTV, as we have seen in this study. The present study showed that three-marker translational setup using the gravity center of three markers is better than one-marker setup for reducing the translational setup error when there is some rotational error. The three-dimensional conformal setup system is expected to be useful for correcting the rotational setup error by adjusting the gantry, couch, and collimator of the linear accelerator to the calculated rotational angles.

Table 1. Mean and standard deviation of the rotation around the $x(\alpha)$, $y(\beta)$, and $z(\gamma)$ axes as estimated by three-dimensional conformal setup

	Average			SD		
Degrees	α	β	γ	α	β	γ
0	−0.3	−1.1	0.6	0.4	0.2	0.3
5	0.4	−0.3	0.0	1.4	0.7	1.4
10	−0.5	0.5	0.8	0.6	0.1	0.7
15	−0.5	0.1	0.6	0.2	0.6	0.4
20	−0.5	0.2	0.7	0.4	0.7	0.5
25	−0.3	0.3	0.4	0.4	0.5	0.6
30	−0.7	0.2	0.6	0.6	0.5	0.6
35	−0.5	−0.2	0.3	0.3	0.1	0.5
40	−0.6	−0.6	0.3	0.2	0.8	0.4
45	−0.7	−0.4	0.2	0.4	0.6	0.6
50	−0.7	−0.2	−0.1	0.2	0.3	0.5
55	−0.4	−0.2	−0.1	0.2	0.1	0.3
60	−0.7	−0.4	0.0	0.4	0.6	0.6
65	−0.3	−0.8	−0.3	0.2	0.3	0.2
70	−0.4	−0.4	−0.6	0.6	0.6	0.2
75	−0.1	−0.7	−0.7	0.5	0.2	0.3
80	−0.6	0.2	−0.3	0.2	0.3	0.5
85	−0.2	−1.1	−1.0	0.9	0.4	0.8
90	−0.2	1.4	−0.7	0.5	0.3	0.1
	−0.4	−0.2	0.0	0.4	0.4	0.5

The present study showed that 3D-CSU is sufficiently accurate for clinical usage provided that the rotating subject is rigid and there is no migration of the markers. However, there are several possible shortcomings of this method. First, the tumors are soft and deformable, so the effect of deformation may mimic the rotation of the subject. Second, migration of the markers can influence the calculation of the rotation angle. Third, if the organ motion in the body is too large, the distance between the skin surface and the tumor's center of gravity changes significantly from the planned beam. In other words, even when 3D-CSU corrected the beam angle's relation to the surface of the tumor, it did not correct the beam angle in relation to the skin surface. Thus, the depth from the skin to the surface of the tumor will change, resulting in a change in dose distribution. The dose to the organs at risk close to the target volume can also change when the corrected beam passes the organs at risk after 3D-CSU. Three-dimensional conformal setup is applicable only when these uncertainties are controllable or taken into account in treatment planning.

Even though its clinical application has limitations, implanting three gold markers method may be useful for certain situations if careful quality control is employed. In practice, the deformation of the tumor and migration of the marker can be estimated based on the distance among three markers to avoid uncertainty. Because the effect of a few millimeters' difference in depth on the absorbed dose is negligible in the case of a megavoltage MV X-ray, the dose to the target volume may not change significantly. Spinal or paraspinal lesions are reasonable candidates for the present version of 3D-CSU since the distance between the skin and the spine does not change significantly. Three markers were attached to the vertebrae during the surgical operation. The steadiness of the marker fixation has been reported previously (2, 6). We have used 3D-CSU for 2 patients with spinal schwannoma in the last year. It was necessary to monitor the disease for more than 3 years to judge the clinical outcome, but there has been no relapse and no adverse effect.

Previous studies have suggested that intrafractional organ motion is negligible in prostate cancer patients in the supine position but can be large in prone position (7). The distance among the three markers was useful to detect the possible migration and deformation of the prostate gland in our previous study (6). Previous studies have suggested that inter-fractional rotational movement of the prostate gland can be so large that 3D-CSU may be usable for prostate cancer (1, 9, 10). Head-and-neck tumors may also benefit from 3D-CSU, as it is often difficult to correct the rotation of the head in the plastic mask attached to the treatment table (11). Uterine cervical cancers may benefit from 3D-CSU as well. For these tumors, reduction of rotational error by 3D-CSU would lead to the reduction in adverse effects and increase in local control rates. For lung tumors, the

intrafractional movement is so large that the benefit of 3D-CSU may be limited unless real-time tumor-tracking of the marker is used during the delivery of the therapeutic beam as well (12).

There have been several attempts to fix the imaging tools onto the gantry of the linear accelerator (13, 14). Although these technologies are promising for the purpose of improving precision radiotherapy, 3D-CSU may not be practical with these configurations because the imaging tools would be obstacles to rotating the table. Our system uses imaging tools on the floor and ceiling so that there is no obstacle to the performance of 3D-CSU as well as to 3D noncoplanar irradiation.

In conclusion, phantom studies showed that 3D-CSU is useful for rotational correction of the target volume without correcting the position of the patient. This method can improve the accuracy of external radiotherapy. However, the uncertainty regarding the deformation of the tissue, migration of the marker, and the change of distance between the surface of the body and the center of gravity of the target volume must all be estimated for this method to be used in clinical practice.

REFERENCES

1. van Herk M, Bruce A, Kroes AP, *et al.* Quantification of organ motion during conformal radiotherapy of the prostate by three dimensional image registration. *Int J Radiat Oncol Biol Phys* 1995;33:1311–1320.
2. Onimaru R, Shirato H, Aoyama H, *et al.* Calculation of rotational setup error using the real-time tracking radiation therapy (RTRT) system and its application to the treatment of spinal schwannoma. *Int J Radiat Oncol Biol Phys* 2003;56: 126–135.
3. Shirato H, Shimizu S, Kitamura K, *et al.* Four-dimensional treatment planning and fluoroscopic real-time tumor tracking radiotherapy for moving tumor. *Int J Radiat Oncol Biol Phys* 2000;48:435–442.
4. Shimizu S, Shirato H, Kitamura K, *et al.* Use of an implanted marker and real-time tracking of the marker for the positioning of prostate and bladder cancers. *Int J Radiat Oncol Biol Phys* 2000;48:1591–1597.
5. Shirato H, Shimizu S, Kunieda T, *et al.* Physical aspects of a real-time tumor-tracking system for gated radiotherapy. *Int J Radiat Oncol Biol Phys* 2000;48:1187–1195.
6. Shirato H, Harada T, Harabayashi T, *et al.* Feasibility of insertion/implantation of 2.0 mm-diameter gold internal fiducial markers for precise setup and real-time tumor-tracking in radiation therapy. *Int J Radiat Oncol Biol Phys* 2003;56:240–247.
7. Kitamura K, Shirato H, Shimizu H, *et al.* Registration accuracy and possible migration of internal fiducial gold marker implanted in prostate and liver treated with real-time tumor-tracking radiation therapy (RTRT). *Radiother Oncol* 2002;62:275–281.
8. Zelefsky MJ, Crean D, Mageras GS, *et al.* Quantification and predictors of prostate position variability in 50 patients evaluated with multiple CT scans during conformal radiotherapy. *Radiother Oncol* 1999;50:225–234.
9. Padhani AR, Khoo VS, Suckling J, *et al.* Evaluating the effect of rectal distension and rectal movement on prostate gland position using cine MRI. *Int J Radiat Oncol Biol Phys* 1999; 44:525–533.
10. Yan Y, Song Y, Boyer AL. An investigation of a video-based patient repositioning technique. *Int J Radiat Oncol Biol Phys* 2002;54:606–614.
11. Kaatee RSJP, Olofsen MJJ, Verstraate MBJ, *et al.* Detection of organ movement in cervix cancer patients using a fluoroscopic electronic portal imaging device and radiopaque markers. *Int J Radiat Oncol Biol Phys* 2002;54:576–583.
12. Seppenwoolde Y, Shirato H, Kitamura K, *et al.* Precise and real-time measurement of 3D tumor motion in lung due to breathing and heartbeat, measured during radiotherapy. *Int J Radiat Oncol Biol Phys* 2002;53:822–834.
13. Jaffray DA, Siewerdsen JH, Wong JW, *et al.* Flat-panel cone-beam computed tomography for image-guided radiation therapy. *Int J Radiat Oncol Biol Phys* 2002;53:1337–1349.
14. Dehnad H, Nederveen AJ, van der Heide UA, *et al.* Clinical feasibility study for the use of implanted gold seeds in the prostate as reliable positioning markers during megavoltage irradiation. *Radiother Oncol* 2003;67:295–302.

Int. J. Radiation Oncology Biol. Phys., Vol. 58, No. 4, pp. 1177–1183, 2004

0360-3016/04/$–see front matter

ELSEVIER

doi:10.1016/j.ijrobp.2003.08.034

CLINICAL INVESTIGATION **Brain**

INTEGRATION OF FUNCTIONAL BRAIN INFORMATION INTO STEREOTACTIC IRRADIATION TREATMENT PLANNING USING MAGNETOENCEPHALOGRAPHY AND MAGNETIC RESONANCE AXONOGRAPHY

HIDEFUMI AOYAMA, M.D., PH.D.,* KYOUSUKE KAMADA, M.D., PH.D.,†
HIROKI SHIRATO, M.D., PH.D.,* FUMIYA TAKEUCHI, PH.D.,‡ SHINYA KURIKI, PH.D.,‡
YOSHINOBU IWASAKI, M.D., PH.D.,† AND KAZUO MIYASAKA, M.D., PH.D.*

Departments of *Radiology and †Neurosurgery, Hokkaido University Graduate School of Medicine; ‡Research Institute of Applied Electricity, Hokkaido University, Sapporo, Japan

Purpose: To minimize the risk of neurologic deficit after stereotactic irradiation, functional brain information was integrated into treatment planning.

Methods and Materials: Twenty-one magnetoencephalography and six magnetic resonance axonographic images were made in 20 patients to evaluate the sensorimotor cortex (n = 15 patients, including the corticospinal tract in 6), visual cortex (n = 4), and Wernicke's area (n = 2). One radiation oncologist was asked to formulate a treatment plan first without the functional images and then to modify the plan after seeing them. The pre- and postmodification values were compared for the volume of the functional area receiving ≥15 Gy and the volume of the planning target volume receiving ≥80% of the prescribed dose.

Results: Of the 21 plans, 15 (71%) were modified after seeing the functional images. After modification, the volume receiving ≥15 Gy was significantly reduced compared with the values before modification in those 15 sets of plans (p = 0.03). No statistically significant difference was found in the volume of the planning target volume receiving ≥80% of the prescribed dose (p = 0.99). During follow-up, radiation-induced necrosis at the corticospinal tract caused a minor motor deficit in 1 patient for whom magnetic resonance axonography was not available in the treatment planning. No radiation-induced functional deficit was observed in the other patients.

Conclusion: Integration of magnetoencephalography and magnetic resonance axonography in treatment planning has the potential to reduce the risk of radiation-induced functional dysfunction without deterioration of the dose distribution in the target volume.

Radiosurgery, Magnetoencephalography, Axon, Function, Arteriovenous malformation.

INTRODUCTION

One of the advantages of stereotactic irradiation (STI) over surgical resection in the treatment of brain diseases is that STI is an easier and safer method of accessing areas deep in the brain, as well as those located in the vicinity of the functional brain cortex. Permanent radiation injury, known as radiation necrosis, is not a common consequence of STI. However, once necrosis occurs in certain areas of the brain responsible for motor function, visual function, comprehension, or speech production, it results in permanent neurologic deficits (1–4). The development of radiation necrosis is related to the dose of radiation received. Considering that neuronal fibers are serial in structure, the severity of the neurologic deficit is expected to be related to factors such as the maximal radiation dose administered to functional brain areas, as well as the volume of the area exposed to more than the threshold dose of radiation (5, 6). Although the threshold dose of radiation required to develop radiation necrosis has not been fully investigated, some clinical and experimental data have indicated that the threshold single dose lies within the range of 10–15 Gy (3, 4, 7).

Recently, imaging modalities that enable the identification of functional brain areas have emerged as clinically significant (8–18). Magnetoencephalography (MEG) is used to detect the magnetic field associated with intracranial neuronal electric activity. In practice, it has been used to identify the sensorimotor, visual, and Wernicke's speech cortices (8, 10–12). Magnetic resonance (MR) axonography or anisotropic diffusion-weighted MRI (ADWI) is a method that visualizes the

Reprint requests to: Hidefumi Aoyama, M.D., Ph.D., Department of Radiology, Hokkaido University Graduate School of Medicine, North-15 West-7, Kita-ku, Sapporo 060-8638, Japan. Tel: (+81) 11-716-1161; Fax: (+81) 11-706-7876; E-mail: hao@radi.med.hokudai.ac.jp

Presented in part at the American Society for Therapeutic Radiology and Oncology (ASTRO) Annual Meeting, New Orleans, LA, October 2002.

Received Feb 4, 2003, and in revised form Aug 11, 2003. Accepted for publication Aug 15, 2003.

Table 1. Patient characteristics and results

Pt. No.	Disease	Age (y)	Follow-up (mo)	Modality	Identified functional area	RT dose (Gy)/ fraction (*n*)	D_{max} (Gy) Functional information		V_{10} (cm^3) Functional information		V_{15} (cm^3) Functional information	
							Yes	No	Yes	No	Yes	No
1	Met	59	29	MEG	Motor cortex	35/4	16.3	18.7	0.9	6.2	0.2	5.3
2	Met	82	4	MEG	Visual cortex	35/4	18.7	19.2	1.7	3.7	0.9	5.5
3	Met	75	5	MEG	Motor cortex	35/4	18.5	19.1	2.46	3.72	1.02	3.48
	Met			MEG	Visual cortex	35/4	11.1	18.5	0.09	0.97	0	0.89
4	AVM	11	31	MEG	Motor cortex	22.5/1	7.0	11.3	0	0.34	0	0
5	AVM	41	23	MEG	Motor cortex	20/1	16.0	16	0.32	0.32	0.16	0.16
6	AVM	26	37	MEG	Motor cortex	35/4	17.4	20.3	2.68	7.68	0.7	3.96
7	AVM	45	31	MEG	Motor cortex	35/4	7.5	9.6	0	0.11	0	0
8	AVM	40	34	MEG	Motor cortex	25/1	9.9	10.1	0	0	0	0
9	AVM	21	27	MEG	Visual cortex	20/4	6.1	9	0.11	0.11	0	0
10	AVM	29	21	MEG	Wernicke's area	25/1	3.7	3.7	0	0	0	0
11	Met	64	8	MEG	Motor cortex	25/1	25.0	26	3.06	4.5	1.98	3.5
12	Met	64	20	MEG	Motor cortex	35/4	16.1	16.1	0.76	0.76	0	0
13	AVM	45	18	MEG+AX	Motor cortex and CST	35/4	12.4	13.8	1.69	1.88	2.6	3.1
14	AVM	60	3	MEG+AX	Motor cortex and CST	35/4	8.0	11.7	1.09	1.59	1.4	0.5
15	AVM	27	13	MEG	Visual cortex	20/1	2.0	2	0	0	0	0
16	AVM	12	9	MEG+AX	Motor cortex and CST	15/1	15.9	15.9	4.68	4.68	0.36	0.36
17	AVM	44	8	MEG	Wernicke's area	35/4	7.3	9.7	0	0	0	0
18	AVM	51	6	MEG+AX	Motor cortex and CST	35/4	0.0	0	0	0	0	0
19	AVM	65	6	MEG+AX	Motor cortex and CST	33/4	14.8	17.2	0	0	0	0
20	AVM	58	6	MEG+AX	Motor cortex and CST	35/4	17.4	18.3	0.35	0.49	0.07	0.14

Abbreviations: Pt. No. = patient number; RT = radiotherapy; D_{max} = maximal dose within functional area converted into single fraction schedule by linear quadratic model; V_{10} or V_{15} = volume of functional area receiving ≥ 10 Gy or ≥15 Gy; Met = metastasis; MEG = magnetoencephalography; AVM = arteriovenous malformation; AX = MR axonography; CST = corticospinal tract.

axonal pathway in the brain. ADWI applies three-orthogonal diffusion gradient pulses and can clearly demonstrate neuronal fibers perpendicular to a diffusion gradient as a hyperintense area. Theoretically, all the subcortical tracts that run in the cranial–caudal direction become hyperintense in the AP diffusion gradient; however, previous reports on ADWI have suggested that the hyperintense areas might consist mainly of the corticospinal tract (16–18).

Integration of the three-dimensional (3D) configuration of functional brain areas into conformal radiotherapy planning using MEG and ADWI may minimize the risk of developing symptomatic adverse effects due to radiation necrosis at the functional brain area. In this study, we evaluated the potential contribution of integrating functional information into radiotherapy planning by dose–volume statistics to reduce the risk of symptomatic radiation necrosis. Preliminary clinical outcomes are also reported.

METHODS AND MATERIALS

Twenty patients (8 females and 12 males, median age, 45 years; range, 11–82 years) with intracranial disease located near or within the functional cortex or corticospinal tract were included in this study. The patient characteristics are listed in Table 1. Five patients had brain metastases and 15 had arteriovenous malformations (AVMs). One of the patients with metastases underwent STI for two lesions; thus, 21 lesions were included. Functional brain areas were identified by MEG in all 21 areas of the 20 patients. Six recent cases in which the lesions were close to the corticospinal tract pathway were evaluated using ADWI as well. Follow-up ranged from 3 to 35 months (mean, 12 months).

The MEG studies were performed in a magnetically shielded room with a 204-channel whole-head biomagnetometer (VectorView, 4D-Neuroimage, San Diego, CA). The spatial resolution of MEG to detect the location of functional cortex is considered to be <5 mm (8–12). For the identification of the sensorimotor cortex in 15 patients, a somatosensory mapping protocol was used in which the median and tibial nerves contralateral to the side of the lesion were stimulated at the wrist and ankles, respectively, with 0.2-ms constant-current pulses. For the primary visual cortex mapping in 4 patients (Fig. 1), the visually evoked field was measured by standard pattern shift stimulation. Wernicke's area was identified by a simple object-naming task in 2 right-handed patients (Fig. 2). In the evaluation of the corticospinal tract using ADWI, hyperintense areas with an intensity 1.6 times greater than that of normal white matter in the AP diffusion gradient were considered as part of the corticospinal tract (Fig. 3). Anatomic, ADWI experiments were performed during MRI investigation using a 1.5-T whole-body MRI scanner with echo-planner capabilities and a standard whole-head transmit-receiver coil (Magnetom Vision, Siemens AG, Erlangen, Germany). Four sessions of multislice, single-shot, spin-echo, echo-planar ADWI (TE, 87 ms; 128 × 128 matrix; 19 slices) were performed with a b value of 1000 s/mm^2. After the raw data of

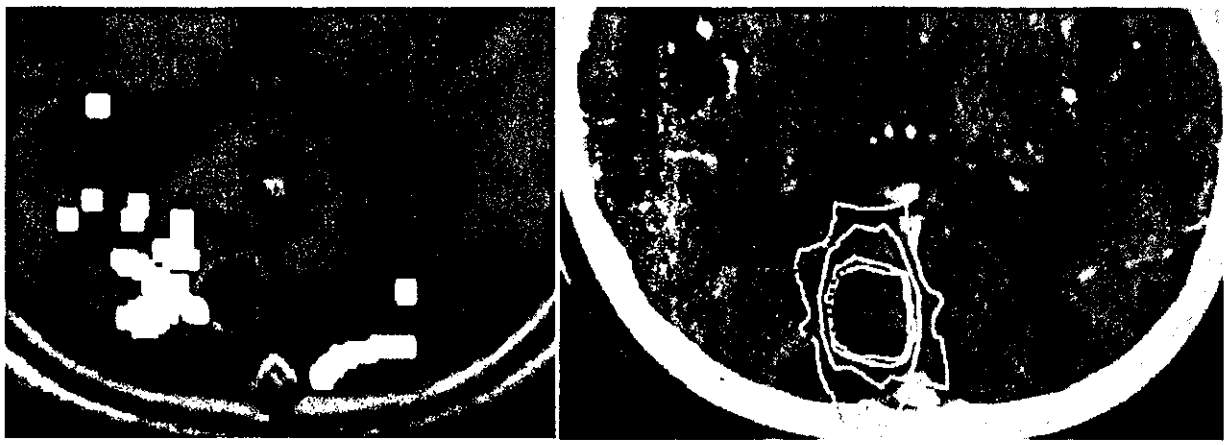

(a) (b)

Fig. 1. Brain metastasis near primary visual cortex (Patient 2). (a) Enhanced MRI with dipoles for primary visual cortex showing normally located left primary visual cortex and dislocated right primary visual cortex by metastasis. (b) Planning target volume (black solid line), primary visual cortex (black dotted line), and isodose lines (white lines, 90%, 80%, 50%, and 30% from inside out).

each ADWI session were two-dimensionally reconstructed, all four sessions of ADWI were averaged. The diffusion gradients were applied sequentially in three orthogonal directions to generate three sets of transverse ADW images to visualize the tract orientation. Because the corticospinal tract was theoretically expected to be the most hyperintense area in the AP diffusion gradient, we took as the corticospinal tract those hyperintense areas having intensity 1.6 times greater than the normal white matter. Anatomic 3D-MRI data of each patient's head was obtained, resulting in 128 sequential, 1.8-mm-thick, axial slices with a resolution of 256 × 256 pixels in a field of view of 300 mm. Data from Both the MEG dipole and the ADWI were integrated into an anatomic 3D-MR image, herein referred to as function-integrated MRI.

The MRI scan can be registered with the CT image using a CT-MRI fusion system (EV pro, Hitachi Medico, Tokyo), as described in detail previously (19). The anatomic CT scan for radiation planning was conducted using a conventional CT

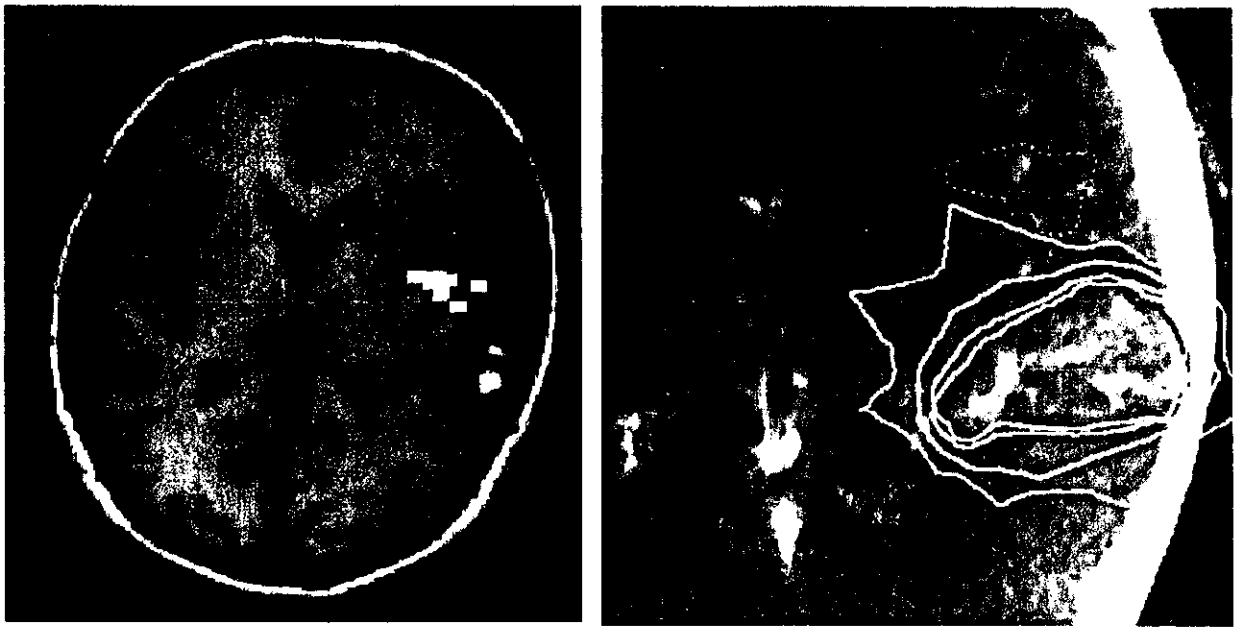

(a) (b)

Fig. 2. Arteriovenous malformation close to Wernicke's area (Patient 17). (a) T_1-weighted MRI with dipoles of magnetoencephalography. (b) Planning target volume (black solid line), Wernicke's area (black dotted line), and isodose lines (white lines, 90%, 80%, 50%, and 30% from inside out).

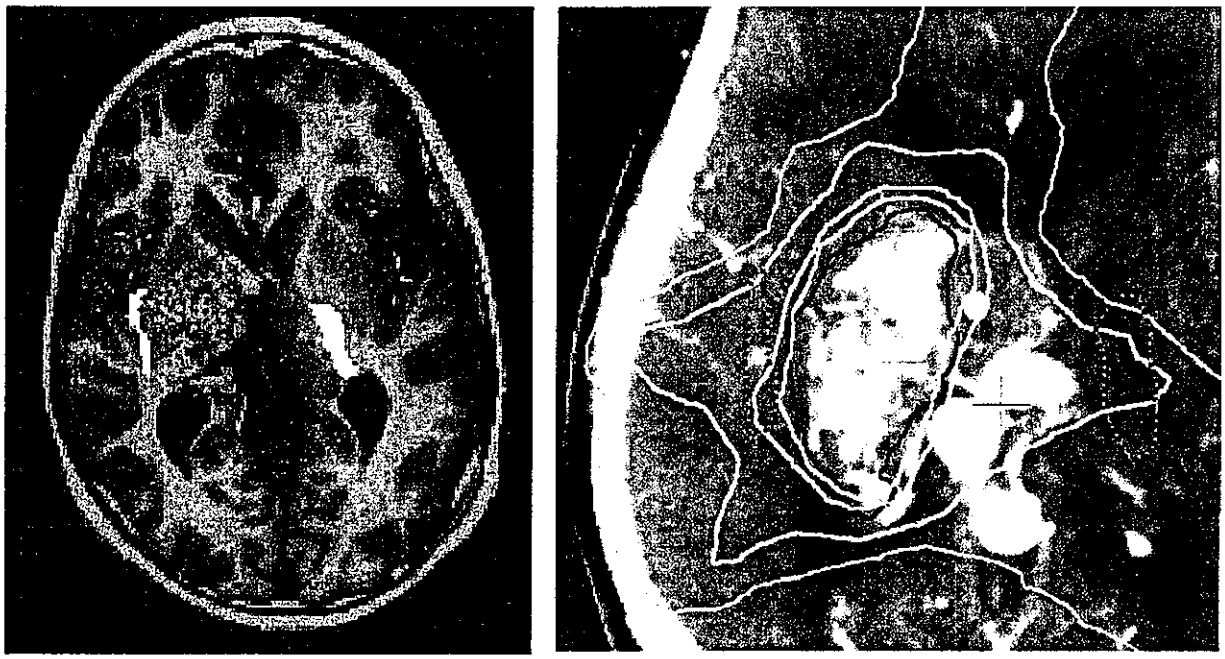

(a) (b)

Fig. 3. Arteriovenous malformation (AVM) close to corticospinal tract (Patient 16). (a) MR axonography showing right corticospinal tract dislocated by large AVM. (b) Planning target volume (black solid line), corticospinal tract (black dotted line), and isodose lines (white lines, 90%, 80%, 50%, and 30% from inside out).

machine (Sfida, SCT-7000TX/TH, Shimazu, Kyoto) with slice thickness of 3 or 5 mm and a matrix size of 256 × 256 with a field of view of 280 mm. In brief, registration of the CT and MRI scans can be conducted on the basis of four or more anatomic landmarks (e.g., the bilateral cochlea, top of the basilar artery, anterior commissure). After the registration, the contoured region-of-interest, such as the tumor or organs at risk on MRI, is automatically superimposed on the relevant CT image. In the same manner, after the registration of the function-integrated MRI with the CT image, the functional area was contoured on MRI and then superimposed on the relevant CT images. The CT images with the contours of the tumors, anatomic organs at risk, and functional area (i.e., function-integrated CT images) can be transferred to a 3D-RTP system (Focus, CMS, St. Louis, MO) and used for dose calculation with inhomogeneity correction. STI was performed with a 6-MV linear accelerator-based stereotactic system (Clinac 2300 C/D, Varian, CA) using treatment parameters transferred via Ethernet. The setup accuracy of the system was estimated to be ±1 mm.

In this study, the treatment plans were first created using conventional MRI-CT fusion images without functional data by one radiation oncologist who was unaware of the information regarding the functional brain areas. After the radiation oncologist had completed the treatment plans, they were modified using function-integrated CT images. We evaluated the influence of the integration of functional information into the planning by comparing the dose–volume statistics between the two consecutive plans for the same patient. The final treatment plans formulated using function-integrated CT were chosen for actual treatment.

Radiation was delivered radiosurgically in a single session to five lesions ranging in isocentric doses from 20 to 25 Gy (median, 20 Gy). Ten other lesions were treated with hypofractionated STI using 20–35 Gy (median, 35 Gy) at the isocenter in four fractions. The planning target volume (PTV) was covered with an 80–90% isodose surface. To simplify the evaluation, each schedule of hypofractionated dose was converted into a single fraction schedule using a linear-quadratic model with an α/β ratio of 2 for normal tissue. The maximal dose (D_{max}) to the functional area and the volume of the functional area receiving ≥10 Gy (V_{10}) and ≥15 Gy (V_{15}) were used to evaluate the effect on the functional area. The dose that 95% of the PTV received and the amount of the PTV receiving ≥80% of the prescribed dose were used to evaluate the effect on the target volume. Student's t test was used for the comparison. Values of $p < 0.05$ were considered to indicate statistical significance.

RESULTS

Dose–volume statistics

The functional cortex was successfully identified in all 21 regions using MEG. The corticospinal tract pathway was also well identified using ADWI in all 6 patients examined. Of the 21 plans, 15 (71%) were judged to have been modified using the function-integrated CT images and only 6 (29%) remained unchanged.

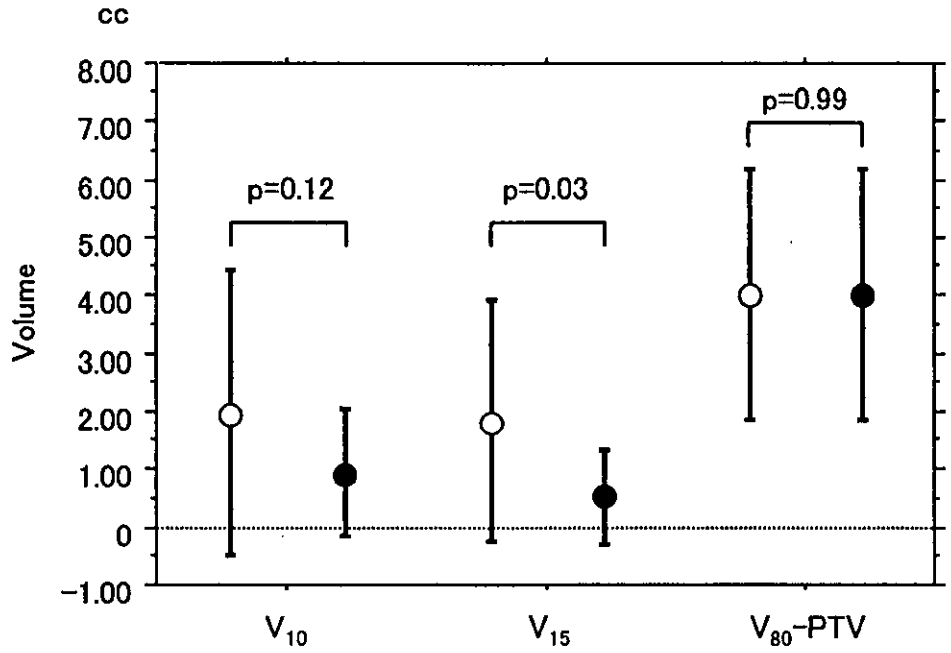

Fig. 4. Volume of functional area receiving ≥10 Gy or ≥15 Gy and amount of planning target volume (PTV) receiving ≥80% of prescribed dose before (white circles) and after (black circles) modification in 15 sets of plans that were changed after seeing the functional information.

In the 15 lesions for which the plan was modified, the D_{max}, V_{10}, and V_{15} of the functional area after the modification were consistently reduced compared with the plan without functional information. The mean D_{max}, V_{10}, and V_{15} before modification was 15.5 Gy, 2.1 cm^3, and 1.8 cm^3, respectively, and was reduced to 13 Gy, 0.9 cm^3, and 0.5 cm^3, respectively, after modification. The reduction was not statistically significant for D_{max} (p = 0.24) or V_{10} (p = 0.12), but it was statistically significant for V_{15} (p = 0.03; Fig. 4). In all 21 lesions, the average D_{max} was 13.7 Gy (SD 6.53) before modification and 12.0 Gy (SD 6.4) after modification (p = 0.41). In total, the V_{10} was 1.8 cm^3 (SD 2.3) before modification and 0.9 cm^3 (SD 1.3) after modification (p = 0.17). The V_{15} was 1.3 cm^3 (SD 1.3) before modification and 0.4 cm^3 (SD 0.7) after modification (p = 0.04).

In the 15 sets of plans that were modified after seeing the functional information, no statistically significant dose reduction was needed in the PTV. The dose that 95% of the PTV received was 18.5 Gy (SD 4.5) before modification and 17.8 Gy (SD 4.0) after modification (p = 0.66). The amount of the PTV receiving ≥80% of the prescribed dose was 4.02 cm^3 (SD 2.15) before modification and 4.02 cm^3 (SD 2.15) after modification (p = 0.99; Fig. 4).

In all 21 sets of plans, no reduction was seen in the PTV after modification, as expected. The mean dose that 95% of the PTV received in the 21 plans was 18.4 Gy (SD 4.2) and 17.9 Gy (SD 3.7) before and after the modification (p = 0.66). The amount of the PTV receiving ≥80% of the prescribed dose was 5.131 cm^3 (SD 5.27) before and 5.132 cm^3 (SD 5.27) after the modification (p = 0.99).

Functional outcome

Adverse events after STI occurred in 4 patients. One patient with AVM had intracranial bleeding and died 3 months after STI (Patient 14). Other adverse events included an increased signal on T_2-weighted MRI in 2 patients (Patients 10 and 13) and radiation necrosis in 1 patient (Patient 4). The former 2 patients did not complain of any neurologic symptoms. The patient with radiation necrosis complained of a minor motor deficit, which showed limitation of movement of the left ankle. This patient had an AVM at the corpus callosum and had undergone MEG but not ADWI before radiosurgery. ADWI was performed when he complained of a motor deficit. It showed radiation injury to the corticospinal pathway (Fig. 5).

DISCUSSION

During the past decade, an increasing body of evidence has indicated that larger doses of radiation lead to better cures of AVM and brain metastases after STI (1, 2, 20, 21). To obtain a cure or local control of disease, coverage of the disease by at least 15 Gy has generally been considered necessary for AVM (1) and ≥18–20 Gy was recommended for brain metastases (20, 21). However, such treatment schedules are consistently accompanied by a 3–7% risk of developing radiation necrosis (1–4, 20, 21). The degree of neurologic deficit is associated with the location and size of the radiation necrosis (3, 4). Therefore, if functional areas are not involved in the high-dose area, patients would be symptom free even if they had radiation necrosis in a silent area. Precise integration of functional images is expected

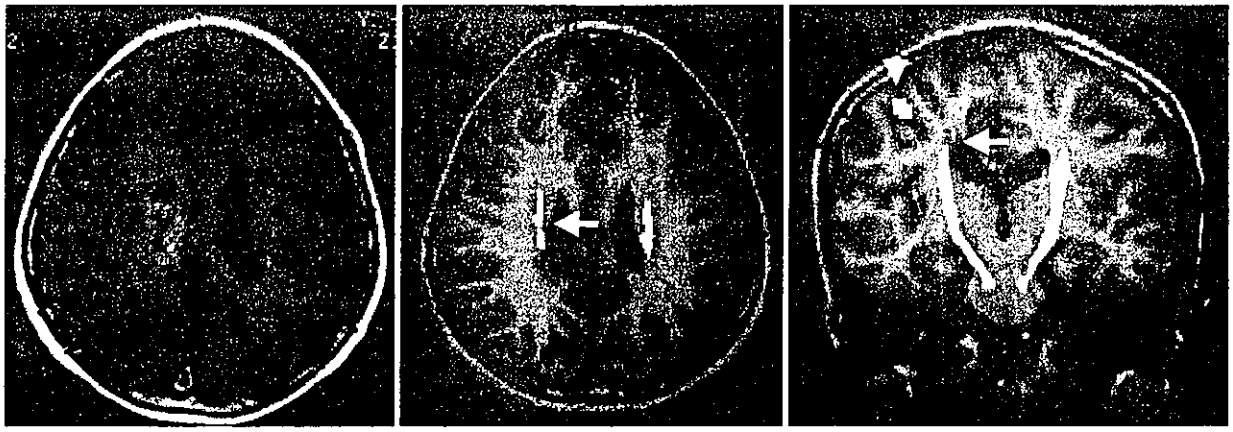

(a) (b) (c)

Fig. 5. Magnetic resonance (MR) axonography after radiation necrosis occurred (Patient 4). (a) Enhanced T_1-weighted MRI. (b) axial view of MR axonography. (c) coronal view of MR axonography showing necrotic area (white arrow) involved in right corticospinal tract, which was far from the dipole of the magnetoencephalography image and consistent with the motor cortex (arrowhead).

not only to reduce radiation injury but also to increase the cure rate for AVMs and tumors by allowing delivery of a sufficient dose without fear of adverse reactions.

Apart from MEG, functional MRI (fMRI) and positron emission tomography are reported to be useful functional imaging modalities. fMRI is used for radiotherapy planning (14, 15). MEG provides the direct measure of neuronal electric activity. Compared with MEG, fMRI and positron emission tomography provide a three-dimensional representation of the functional activity in the brain in terms of metabolic and hemodynamic variables. However, the relationship between those variables and neuronal activity has not yet been well defined. Although fMRI can localize the functional cortex, its efficacy and validity for AVMs are reported to be low (13). The major issue is that functional brain mapping by fMRI is based on hemodynamic changes, and thus it might be affected if autoregulation of the blood flow is lost in the brain tissue near the AVM. In contrast, MEG detects the magnetic field associated with intracranial neuronal electric activity itself and thus is not influenced by a high blood flow shunt (13). Therefore, it is reasonable to use MEG in patients with AVMs (13). ADWI, which visualizes the axonal pathway in the brain, has emerged as a potentially useful tool to supplement these images (16–18). Kamiryo *et al.* (13) recently developed a technique combining MEG data and angiography as a tool to provide simultaneous viewing of both modalities in three dimensions. They reported that this technique may reduce the risks associated with embolization treatment (13). A group in New Jersey used fMRI for radiosurgical planning and succeeded in reducing the D_{max} to the functional area in 3 patients in the treatment planning with an average dose reduction of 32% (14, 15).

In the present series, MEG was used in 21 regions in 20 patients to localize the sensorimotor cortex, visual cortex, and Wernicke's area. We also used ADWI in addition to MEG in the 6 most recent patients. Dose–volume histogram analysis revealed that the area of functional brain tissue receiving 15 Gy was significantly reduced when plans were modified after the functional information was provided, and the coverage of the PTV did not significantly deteriorate. One patient with an AVM at the corpus callosum who did not undergo ADWI experienced a minor motor deficit, indicating that functional imaging of the relevant cortex is not sufficient to reduce symptomatic complications. Injury to the corticospinal tract was suggested to be reduced with the use of ADWI.

CONCLUSION

We have developed a method of integrating information about the functional cortex and corticospinal tract into STI planning. Although additional investigation is necessary to understand fully the contribution of functional imaging studies, the results presented here indicate that the integration of functional brain information could potentially reduce the risk of developing neurologic functional disturbance after undergoing STI.

REFERENCES

1. Touboul E, Al Halabi A, Buffat L, *et al.* Single-fraction stereotactic radiotherapy: A dose-response analysis of arteriovenous malformation obliteration. *Int J Radiat Oncol Biol Phys* 1998;41:855–861.
2. Aoyama H, Shirato H, Nishioka T, *et al.* Treatment outcome of single or hypofractionated stereotactic irradiation (STI) using a linear accelerator for intracranial arteriovenous malformation. *Radiother Oncol* 2001;59:323–328.
3. Flickinger JC, Kondziolka D, Lunsford LD, *et al.* Development of a model to predict permanent symptomatic postradiosurgery. *Int J Radiat Oncol Biol Phys* 2000;46:1143–1148.
4. Voges J, Treuer H, Sturm V, *et al.* Risk analysis of linear

radiosurgery. *Int J Radiat Oncol Biol Phys* 1996;36:1055–1063.
5. Kallman P, Agren A, Brahme A. Tumour and normal tissue responses to fractionated non-uniform dose delivery. *Int J Radiat Biol* 1992;62:249–262.
6. Niemierko A, Goitein M. Modeling of normal tissue response to radiation: The critical volume model. *Int J Radiat Oncol Biol Phys* 1992;25:135–145.
7. Fike JR, Cann CE, Turowski K, *et al.* Radiation dose response of normal brain. *Int J Radiat Oncol Biol Phys* 1998;14:63–70.
8. Kamada K, Takeuchi F, Kuriki S, *et al.* Functional neurosurgical stimulation with brain surface magnetic resonance images and magnetoencephalography. *Neurosurgery* 1993;33:269–273.
9. Schulder M, Maldjian JA, Liu WC, *et al.* Functional image-guided surgery of intracranial tumors located in or near the sensorimotor cortex. *J Neurosurg* 1998;89:412–418.
10. Ganslandt O, Fahlbusch R, Nimsky C, *et al.* Functional neuronavigation with magnetoencephalography: Outcome in 50 patients with lesions around the motor cortex. *J Neurosurg* 1999;91:73–79.
11. Kamada K, Kober H, Saguer M, *et al.* Response to silent *Kanji* reading of the native Japanese and German in task subtraction magnetoencephalography. *Cognitive Brain Res* 1998;7:89–98.
12. Alberstone CD, Skirboll SL, Benzel EC, *et al.* Magnetic source imaging and brain surgery: Presurgical and intraoperative planning in 26 patients. *J Neurosurg* 2000;92:79–90.
13. Kamiryo T, Cappell J, Kronberg E, *et al.* Interactive use of cerebral angiography and magnetoencephalography in arteriovenous malformations: Technical note. *Neurosurgery* 2002;50:903–911.
14. Liu WC, Schulder M, Narra V, *et al.* Functional magnetic resonance imaging aided radiation treatment planning. *Med Phys* 2000;27:1563–1572.
15. Shulder M, Vega J, Narra V, *et al.* Functional magnetic resonance imaging and radiosurgical planning. *Stereotact Funct Neurosurg* 1999;73:38–44.
16. Nakada T, Nakayama N, Fujii Y, *et al.* Clinical application of three-dimensional anisotropy contrast magnetic resonance axonography. *J Neurosurg* 1999;90:791–795.
17. Karibe H, Shimizu H, Tominaga T, *et al.* Diffusion-weighted magnetic resonance imaging in the early evaluation of corticospinal tract injury to predict functional motor outcome in patients with deep intracerebral hemorrhage. *J Neurosurg* 2000;95:58–63.
18. Holodny AI, Ollenschleger MD, Liu WC, *et al.* Identification of the corticospinal tracts achieved using blood-oxygen-level-dependent and diffusion functional MR imaging in patients with brain tumors. *AJNR Am J Neuroradiol* 2001;22:83–88.
19. Aoyama H, Shirato H, Nishioka T, *et al.* Magnetic resonance imaging (MRI) system for three-dimensional conformal radiotherapy (3D-CRT) and its impact on gross tumor volume (GTV) delineation of central nervous system (CNS) tumors. *Int J Radiat Oncol Biol Phys* 2001;50:821–827.
20. Shiau CY, Sneed PK, Shu HKG, *et al.* Radiosurgery for brain metastases: Relationship of dose and pattern of enhancement to local control. *Int J Radiat Oncol Biol Phys* 1997;37:375–383.
21. Pirzkall A, Debus J, Lohr F, *et al.* Radiosurgery alone or in combination with whole-brain radiotherapy for brain metastases. *J Clin Oncol* 1998;16:3563–3569.